OPEN ACCESS
IOP Publishing
Journal of Physics G: Nuclear and Particle Physics
J. Phys. G: Nucl. Part. Phys. **51** (2024) 065104 (16pp)
https://doi.org/10.1088/1361-6471/ad3c5b

Cross sections of neutral-current neutrino scattering on ^{98,100}Mo isotopes

R Sahu[1], V K B Kota[2] and T S Kosmas[3,*]

[1] National Institute of Science and Technology, Palur Hills, Berhampur 761 008, Odisha, India
[2] Physical Research Laboratory, Ahmedabad 380 009, India
[3] Department of Physics, University of Ioannina, GR 45110 Ioannina, Greece

E-mail: rankasahu@gmail.com, vkbkota@prl.res.in and hkosmas@uoi.gr

Received 22 December 2023, revised 24 March 2024
Accepted for publication 9 April 2024
Published 30 April 2024

Abstract

Coherent elastic neutrino–nucleus scattering (CEνNS) is a neutral-current low-energy electro-weak reaction-channel detected recently by the COHERENT experiment at the Oak Ridge National Laboratory (ORNL), USA, in the Spallation Neutron Source facility. The extremely weak signal on the CsI detector of the first experiment and on the liquid Ar of the repeated COHERENT experiment is the energy-recoil due to the neutrino–nucleus interaction, where the nucleus is elastically scattered as a whole while simultaneously the neutrino goes out. Today, several promising nuclear detectors are on the way to be employed in designed and ongoing experiments. In our present work, we provide predictions for incoherent scattering cross sections of low-energy neutrinos on ^{98,100}Mo isotopes obtained with the deformed shell model employed previously for similar predictions in other electroweak processes. We mention that, Mo detector medium has been used previously in the MOON and NEMO double beta decay experiments.

Keywords: coherent scattering, neutral current, neutrino–nucleus reactions, deformed shell model, Incoherent cross sections, molibdenium (Mo) isotopes

* Author to whom any correspondence should be addressed.

1. Introduction

During the past few decades, neutrinos, the most abundant and least understood particles in nature, have attracted much attention from researchers in nuclear physics, astroparticle physics, and cosmology [1–4]. Currently, many extremely sensitive worldwide neutrino experiments [5] with ultra-high precision detectors aim to measure different types of neutrino properties, neutrino-matter interactions as well as open problems related to standard and non-standard neutrino physics involving neutral- and charged-current neutrino–nucleus processes.

Some years ago (September 2017), the neutral-current neutrino–nucleus channel was detected for the first time in the ORNL COHERENT experiment [5], 43 years after its theoretical prediction by Freedman [1]. The measurement of coherent elastic event rates of neutrino scattering on a sodium doped CsI detector may help in answering some key questions related to neutrino properties and provide an understanding of some theories beyond the standard model (BSM) of the electroweak interactions [4]. The produced nuclear energy-recoil signals are appreciably weak and that is why the first measurement of CEνNS events was considerably delayed after its first proposal and was finally observed at the Oak Ridge National Laboratory by the COHERENT Collaboration [5].

The neutrino beam employed by the COHERENT experiment was produced through pion-decay-at-rest (π-DAR neutrino beam) coming from the spallation neutron source facility (SNS) of ORNL. The first COHERENT measurement was performed by using a CsI detector [5, 6] and, subsequently, using a liquid argon detector [7]. Currently, other important CEνNS experiments, mainly based on Nuclear power plant neutrinos, are in operation such as NCC-1701 [8], CONNIE [9], CONUS [10], and νGeN [11]. In addition, there are also experiments in preparation as the MINER [12], Chooz [13], the ν-Cleus [14], the TEXONO [15], the RICOCHET [16], the νIOLETA [17] and Scintillating Bubble Chamber (SBC) [18], European spallation source [19]. We note that, the nuclear power plant facilities have the advantage of producing an extremely intense beam of low-energy ($E_\nu < 10$ MeV) antineutrinos.

The observation of neutral-current neutrino–nucleus scattering events opened new windows that may reveal novel aspects of neutrino physics. In addition, the first dark matter search results from coherent CAPTAIN-Mills were measured recently [20]. The neutrino–nucleus cross sections play a crucial role in unraveling the various processes BSM scenarios and in constraining the parameters entering various theories [4]. Up to now, neutral-current ν-nucleus cross section measurements are available for few nuclear reactions.

Theoretically, the nuclear responses of the neutrino-detectors to the energy spectra of observed neutrino fluxes could be simulated by convoluted cross sections obtained by using realistic description for the neutrino energy distribution of the studied neutrino source [21].

On the other hand, neutral-current neutrino–nucleus scattering is independent of the neutrino flavour and can, therefore, be adopted also for studying muon and tau neutrinos occurring in the interior of a supernova (SN) [22]. Neutral-current nuclear detectors for neutrinos from Supernovae [23, 24] could be used to test current supernova models and to study neutrino oscillations. Also, very recently, the detection of supernova, solar, as well as atmospheric neutrinos through coherent neutrino–nucleus scattering became a promising new physics probe with the detector of RES-NOVA project [25, 26]. In this proposal, an array of archaeological lead (Pb) based cryogenic detectors are proposed to be employed since, due to the very large neutron number of Pb isotopes, the CEνNS cross section on Pb is high [25]. Furthermore, the ultrahigh radio-purity of archaeological Pb enables the operation of a high statistics experiment.

The purpose of this work is to study neutral-current neutrino scattering on the ^{98,100}Mo isotopes. The calculations presented are based on the Donnelly–Walecka method [27, 28] which has extensively been employed previously for the treatment of semi-leptonic processes in nuclei. In general, accurate description of the initial and final nuclear states is a key ingredient in realistic neutrino–nucleus scattering calculations and, in this work, the deformed shell model [29] is adopted for computing coherent and incoherent cross sections of neutral-current neutrino–nucleus scattering on the even–even ^{98,100}Mo isotopes.

It should be noted that, cross sections for neutrino scatterings off the stable ($A = 92$, 94, 95, 96, 97, 98, 100) molybdenum isotopes have been previously calculated with the microscopic quasi-particle model (MQPM) that could be applied to other nuclear systems as well [30]. Furthermore, the ^{100}Mo nucleus is a famous double-beta-decay emitter [31, 32] and has been employed by various experiments, e.g. the NEMO Observatory [33], the MOON experiment [34], etc. Thus, nuclear-structure calculations in the Mo region are welcome for other processes and experiments too. The obtained nuclear wave functions [35] are essential in studies of weak processes in ^{100}Mo and in the other stable molybdenum nuclei.

For the odd isotopes ^{95,97}Mo, in [35, 36] the MQPM model was used for the construction of the nuclear states. A similar work for the even–even Mo isotopes has been performed by employing the quasi-particle random phase approximation [32, 37]. In the latter calculations the construction of vibrational states in heavy open-shell nuclei (like the Mo isotopes) is also feasible. Such contributions are not included in the present work due to the limited valence spaces used in nearly all versions of Shell Model.

In the case of the incoherent neutrino–nucleus scattering, the cross sections are derived from these wave functions. It should be mentioned that, in order to obtain realistic estimates for the nuclear responses to the spectra of various neutrino sources, the computed DSM cross sections must be folded with the corresponding neutrino distribution of the neutrino source in question [3, 23, 24].

The rest of this paper is organized as follows. In section 2, the relevant formalism is briefly described, while in section 3 the main assumptions of the Deformed Shell Model employed for the calculations are presented. In section 4, the calculated results of this work are presented and discussed in conjunction with the existing experimental data as well as with the previously published results of other methods. Finally, the extracted findings of our present work are summarized in section 5.

2. Brief description of the related formalism

The details of the relevant formulation that provides the neutral current ν-nucleus scattering differential cross sections have been discussed earlier in [23, 27, 28]. For completeness, we give here a few important steps. The weak interaction neutrino–nucleus Hamiltonian H_I in the low energy domain is written in the effective current-current form as

$$\hat{H}_I = -\frac{G}{\sqrt{2}} \int \mathrm{d}^3x \hat{j}_\mu^{\mathrm{lept}}(\mathbf{x}) \hat{\mathcal{J}}^\mu(\mathbf{x}). \tag{1}$$

In the above, $\hat{j}_\mu^{\mathrm{lept}}$ and $\hat{\mathcal{J}}^\mu$ denote the leptonic and hadronic currents, respectively, and G is the Fermi weak coupling constant.

The double differential cross section for the ν-nucleus scattering from the initial state $|i\rangle \equiv |J_i^\pi M_i\rangle$ to the excited state $|f\rangle \equiv |J_f^\pi M_f\rangle$ is written as

$$\frac{\mathrm{d}^2\sigma_{i\to f}}{\mathrm{d}\Omega\mathrm{d}\omega} = (2\pi)^4\epsilon_f^2 \sum_{s_f,s_i,M_f M_i} \frac{|\langle f|\hat{H}_I|i\rangle|^2}{(2J_i+1)}. \tag{2}$$

Applying a multipole analysis on the weak hadronic currant [27, 28], the cross section given by equation (2) becomes

$$\frac{\mathrm{d}^2\sigma_{i\to f}}{\mathrm{d}\Omega\mathrm{d}\omega}(\phi,\,\theta,\,\omega,\,\epsilon_i) = \delta(E_f - E_i - \omega)\frac{2G^2\epsilon_f^2\cos^2(\theta/2)}{\pi(2J_i+1)}[C_V + C_A \mp C_{VA}]. \tag{3}$$

The δ-function on the right-hand side of the above equation ensures the energy conservation, so that the excitation energy of the nucleus ω is given by

$$\omega = E_f - E_i = \epsilon_i - \epsilon_f. \tag{4}$$

E_i and E_f represent the energy of the initial and final states of the studied nucleus, ϵ_i and ϵ_f are the incoming and outgoing energies of the neutrino. In equation (3), the $(-)$ sign corresponds to the scattering of the neutrinos and the $(+)$ to the scattering of the antineutrinos.

The terms C_V and C_A include a summation over the contributions coming from the polar-vector and axial-vector multipole operators, respectively, as

$$\begin{aligned} C_{V(A)} = &\sum_{J=0}^{\infty}|\langle J_f||\hat{M}_J^{(5)}(q) + \frac{\omega}{q}\hat{L}_J^{(5)}(q)||J_i\rangle|^2 \\ &+ \sum_{J=1}^{\infty}\left(-\frac{q_\mu^2}{2q^2} + \tan^2\frac{\theta}{2}\right)[|\langle J_f|||\hat{T}_J^{\mathrm{mag}(5)}(q)||J_i\rangle|^2 \\ &+ |\langle J_f||\hat{T}_J^{el(5)}(q)||J_i\rangle|^2]. \end{aligned} \tag{5}$$

In the latter equation, the superscript 5 refers to the axial vector components of the hadronic current. The interference term C_{VA} in equation (3) contains the product of transverse polar-vector and transverse axial-vector matrix elements as

$$\begin{aligned} C_{VA} = &2\tan\frac{\theta}{2}\left(-\frac{q_\mu^2}{q^2} + \tan^2\frac{\theta}{2}\right)^{1/2} \\ &\times\sum_{J=1}^{\infty} Re\langle J_i||\hat{T}^{\mathrm{mag}}_J(q)||J_i\rangle\langle J_f||\hat{T}^{el}_J(q)||J_i\rangle^*. \end{aligned} \tag{6}$$

For normal parity transitions, C_{VA} contains contributions of $\hat{T}_J^{el}$ and $\hat{T}_J^{\mathrm{mag5}}$ operators while for abnormal parity ones it contains matrix elements of $\hat{T}_J^{\mathrm{mag}}$ and $\hat{T}_J^{el5}$.

The square of the four-momentum transfer q_μ^2 and the magnitude of the three-momentum transfer $q \equiv|\mathbf{q}|$ can be written in terms of the kinetmatical parameters, i.e. laboratory scattering angle θ and the neutrino energies $\epsilon_i = \epsilon_\nu$ and $\epsilon_f = (\epsilon_i - \omega)$ as

$$\begin{aligned} q_\mu^2 \equiv q_\mu q^\mu &= -4\epsilon_i(\epsilon_i - \omega)\sin^2(\theta/2) \\ q \equiv |\mathbf{q}| &= [\omega^2 + 4\epsilon_i(\epsilon_i - \omega)\sin^2(\theta/2)]^{1/2}. \end{aligned} \tag{7}$$

The reduced matrix elements in equations (5) and (6) are evaluated using the deformed shell model (DSM) as described below. The definitions of the multiple operators are given in the appendix.

The weak nucleon form factors F_i^Z, $i = 1, 2$ entering the multipole operators (see appendix) are expressed in terms of the well known charge and electromagnetic form factors for proton $F_{1,2}^p$ and neutron $F_{1,2}^n$ (conserved vector current, CVC-theory) [28], as

$$F_{1,2}^{Z(p,n)} = \left(\frac{1}{2} - \sin^2\theta_W\right) F_{1,2}^{p,n}\,\tau_0 - \sin^2\theta_W F_{1,2}^{p,n}. \tag{8}$$

The superscript Z refers to the processes with Z-boson exchange. θ_W is the Weinberg angle, $\sin^2\theta_W = 0.2325$. $\tau_0 = +1$ for protons and $= -1$ for neutrons. The Dirac and Pauli form factors F_1 and F_2 for proton and neutron are given in [38] which are $F_1^p = 1$ and $F_2^p = k_p$, $F_1^n = 0$ and $F_2^n = k_n$. The anomalous magnetic moments k_p and k_n are related to the magnetic moments of proton and neutron by $k_p = \mu_p - 1$ and $k_n = \mu_n$, where $\mu_p = 2.7928\ \mu_N$ and $\mu_n = -1.9130\ \mu_N$.

The neutral current axial-vector form factor F_A^Z is given by

$$F_A^Z = \frac{1}{2} F_A(q_\mu^2)\tau_0. \tag{9}$$

Employing the dipole ansatz, we use the static value for $F_A(q_\mu^2)$, i.e. $F_A(q_\mu^2) = g_A = -1.258$, so that

$$F_A^Z = \frac{1}{2}(-1.258)\tau_0. \tag{10}$$

We note that, in the present work, the quenching effect on the axial vector form factor g_A is explicitly taken into consideration (see discussion of the results below).

3. Deformed shell model

The details of this model have been described in many of our earlier publications, see for example [29]. In this model, for a given nucleus, starting with a model space consisting of a given set of single particle (sp) orbitals and effective two-body Hamiltonian (TBME + spe), the lowest energy intrinsic states are obtained by solving the axially symmetric Hartree–Fock (HF) single particle equation self-consistently. Excited intrinsic configurations are obtained by making particle-hole excitations over the lowest intrinsic state. These intrinsic states $\chi_K(\eta)$ do not have definite angular momenta. Hence, states of good angular momentum projected from an intrinsic state $\chi_K(\eta)$ can be written in the form

$$\psi_{MK}^J(\eta) = \frac{2J+1}{8\pi^2\sqrt{N_{JK}}} \int \mathrm{d}\Omega D_{MK}^{J^*}(\Omega) R(\Omega) |\chi_K(\eta)\rangle. \tag{11}$$

where N_{JK} is the normalization constant given by

$$N_{JK} = \frac{2J+1}{2} \int_0^\pi \mathrm{d}\beta \sin\beta d_{KK}^J(\beta) \langle\chi_K(\eta)|\mathrm{e}^{-\mathrm{i}\beta J_y}|\chi_K(\eta)\rangle. \tag{12}$$

In equation (11), Ω represents the Euler angles (α, β, γ), $R(\Omega)$ which is equal to $\exp(-\mathrm{i}\alpha J_z)$ $\exp(-\mathrm{i}\beta J_y)$ $\exp(-\mathrm{i}\gamma J_z)$ represents the general rotation operator.

The good angular momentum states projected from different intrinsic states are not in general orthogonal to each other. Hence they are orthonormalized and then band mixing calculations are performed. The resulting eigenfunctions are of the form

$$|\Phi_M^J(\eta)\rangle = \sum_{K,\alpha} S_{K\eta}^J(\alpha) |\psi_{MK}^J(\alpha)\rangle. \tag{13}$$

The reduced matrix elements occurring in equations (5) and (6) are evaluated using the DSM wave function $\Phi_M^J(\eta)$ defined in equation (13). Towards this purpose we have to first calculate the reduced single particle matrix elements of the relevant operator in the single particle space. The detailed form of the seven operators M_{JM}^{Coul}, Δ_M^J, $\Delta_M'^J$, Ω_M^J, Σ_M^J, $\Sigma_M'^J$ and $\Sigma_M''^J$ are

given in appendix and are also given in [21, 28]. These operators are linearly independent due to CVC theory. Their reduced matrix elements in the single particle space which are of the form $\langle j_1||T_i^J||j_2\rangle$ where T_i^J represent any of these basic tensor multipole operators, have been written in closed compact formulas [21] as

$$\langle j_1||T^J||j_2\rangle = \mathrm{e}^{-y} y^{\beta/2} \sum_{\mu=0}^{\eta_{\max}} \mathcal{P}_{\mu}^{\mathcal{J}} y^{\mu}. \tag{14}$$

where the geometrical coefficients $\mathcal{P}_{\mu}^{\mathcal{J}}$ are rational numbers or square root of rational numbers throughout the model space.

4. The low-lying deformed shell model collective bands in ^{98,100}Mo isotopes

The DSM calculations are performed in the spirit of spherical shell model where one takes a model space and a suitable effective interaction (single-particle orbitals, single-particle energies, and a two-body effective interaction). This procedure has been found to be quite successful in describing the spectroscopic properties and electromagnetic properties of many nuclei in the mass region $A = 60$–90 and has also been applied to double beta decay nuclear transition matrix elements [29]. In addition, this model has recently been used to describe many weak interaction processes [39–44].

In the present calculations for ^{98,100}Mo isotopes, we have adopted the effective interaction *GWBXG* with the ^{66}Ni as the closed core. The details regarding the construction of the effective interaction have been discussed in [45]. The active proton orbits are $0f_{5/2}$, $1p_{3/2}$ $1p_{1/2}$ and $0g_{9/2}$ with single particle energies -5.322, -6.144, -3.941 and -1.250 MeV. For the neutrons, the active orbits are $1p_{1/2}$, $0g_{9/2}$, $0g_{7/2}$, $1d_{5/2}$, $1d_{3/2}$, $2s_{1/2}$. The single particle energies for the first five orbits are taken to be -0.696, -2.597, 5.159, 1.830, 4.261 MeV, respectively. The $2s_{1/2}$ orbit produces low-lying large deformed solutions even though molybdenum isotopes are known to be weakly deformed. Hence, the effect of this orbit is eliminated by taking the corresponding neutron single particle energy at a high value.

Using the above effective interaction and the single particle energies, we first carried out an axially symmetric HF calculation by solving the HF equation self consistently. The single particle spectra corresponding to lowest energy prolate and oblate configurations for the two isotopes ^{98}Mo and ^{100}Mo are shown in figures 1 and 2, respectively. The intrinsic quadrupole moments for both the configurations are small. In our band mixing calculation for positive parity, the intrinsic states with excitation from $1p_{1/2}$ orbital is not considered since such intrinsic states lie very high in energy. Hence essentially our core is also ^{68}Ni. However for negative parity, we have to make one particle excitation from $1p_{1/2}$ since all other neutron orbitals have positive parity.

For ^{98}Mo, the prolate and oblate HF solutions are almost degenerate, with the oblate solution being lower by $\sim$0.3 MeV. We obtained excited HF configurations by making particle-hole excitations over these lowest HF configurations. For positive parity, we consider 30 intrinsic configurations (15 oblate and 15 prolate) and for negative parity 20 intrinsic configurations (10 oblate and 10 prolate).

As described before, good angular momentum states are projected from each of these intrinsic states. These states are not orthogonal to each other. Hence, first, they are orthonormolized and, then, are classified into different bands. States having similar structure and, thus, similar electromagnetic properties are classified into one band. For ^{98}Mo, not many collective bands have been observed. In figure 3, we compare the calculated ground band with the experimentally observed band and we see that the agreement is reasonable.

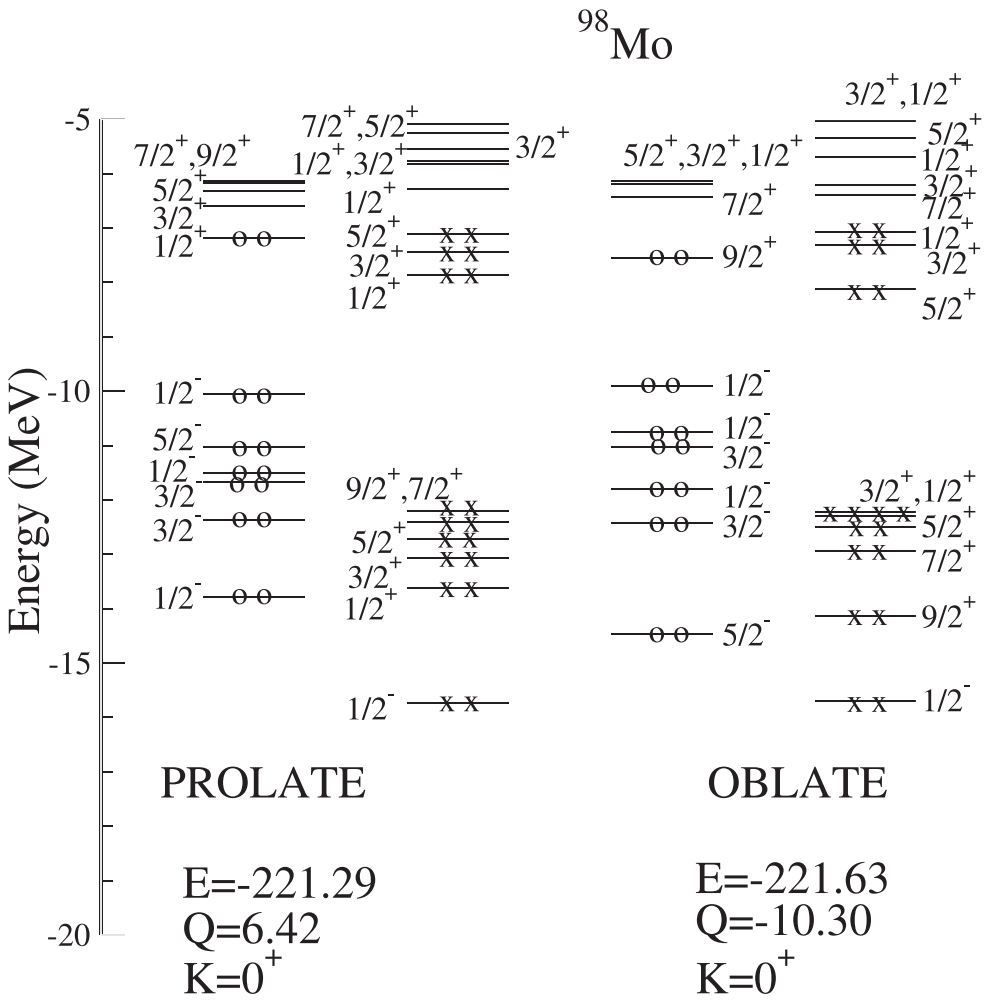

Figure 1. HF single-particle spectra for ^{98}Mo corresponding to lowest energy prolate and oblate configurations. In the figure, circles represent protons and crosses represent neutrons. The HF energy E in MeV, mass quadrupole moment Q in units of the square of the oscillator length parameter and the total azimuthal quantum number K are given in the figure.

For ^{100}Mo, also the prolate and oblate configurations are almost degenerate differing by 0.5 MeV, with the oblate solution being lower. The excited HF configurations are obtained by making particle-hole excitations over these lowest configurations. For positive parity, we consider 33 intrinsic configurations (19 oblate and 14 prolate) and for negative parity 27 intrinsic configurations (14 oblate and 13 prolate). As before, states of good angular momenta are projected from each of these intrinsic states and, then, a band mixing calculation is performed.

The band mixed levels are classified into different bands on the basis of their $E2$ connectivity. The experimentally observed collective bands are in good agreement with experiment as shown in figure 4. Our calculations have also many other low-lying levels (not shown in the figure) which can be compared with the observed levels presented in [46].

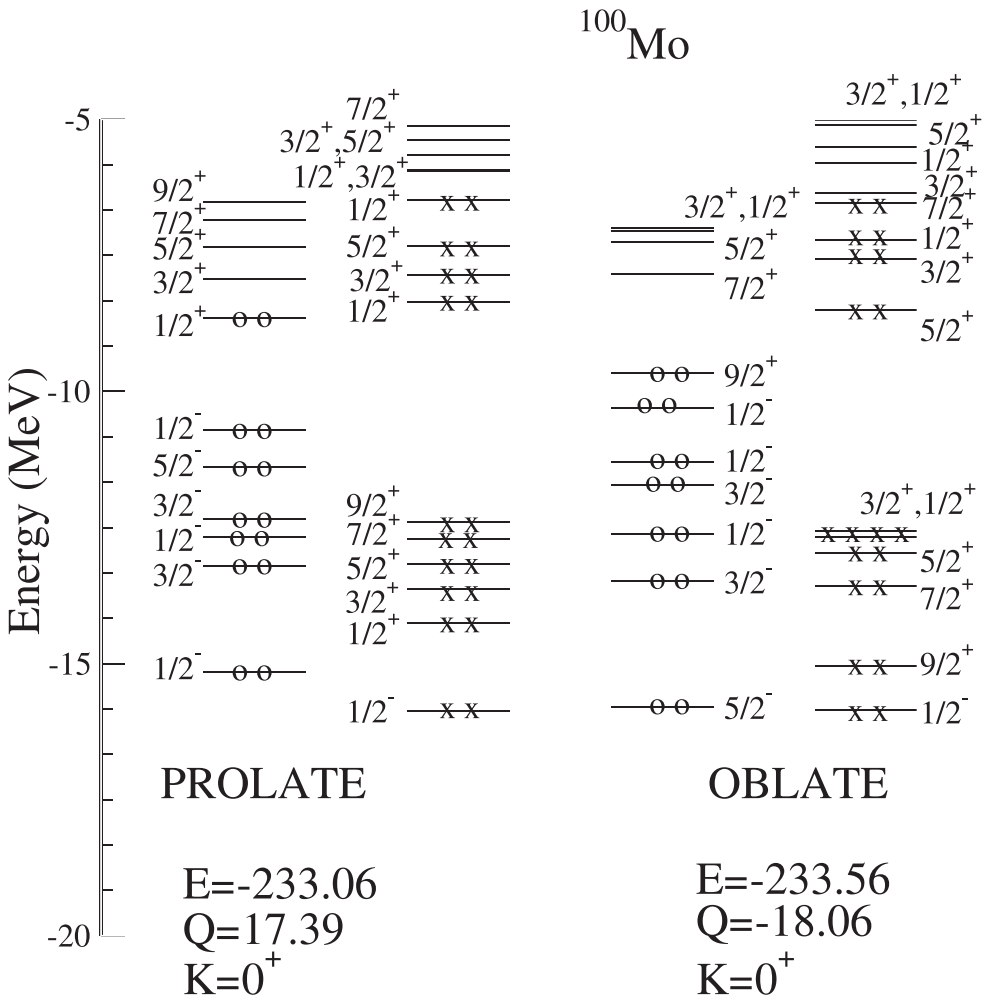

Figure 2. HF single-particle spectra for ^{100}Mo corresponding to lowest energy prolate and oblate configurations. In the figure, circles represent protons and crosses represent neutrons. The HF energy E in MeV, mass quadrupole moment Q in units of the square of the oscillator length parameter and the total azimuthal quantum number K are given in the figure.

Going beyond the energy spectra, the calculated magnetic moments for the 2_1^+ states of ^{98}Mo and ^{100}Mo are 1.30 and 1.35 μ_N respectively and they are obtained using bare gyromagnetic ratios. The corresponding experimental values from [46] are 0.97 ± 0.06 and 0.94 ± 0.07 μ_N respectively and they agree quite well with the calculated values. Still better agreements can be obtained by using effective gyromagnetic ratios which are used by many groups; see for example [47]. Turning to $B(E2)$ values, the experimental values for the transitions $2_1^+ \rightarrow 0_1^+$ and $4_1^+ \rightarrow 2_1^+$ are 37.6 and 69 Wu respectively for ^{100}Mo and 20 and 42 Wu respectively for ^{98}Mo. The calculated $B(E2)$ values for the above transitions are 19 and 28 Wu respectively for ^{100}Mo which are off from the experimental values by a factor of $\sim$2. Same is the situation with ^{98}Mo with values 16 and 15 Wu. The calculation of $B(E2)$'s requires effective charges so as to take into account the effect of the core polarization effects.

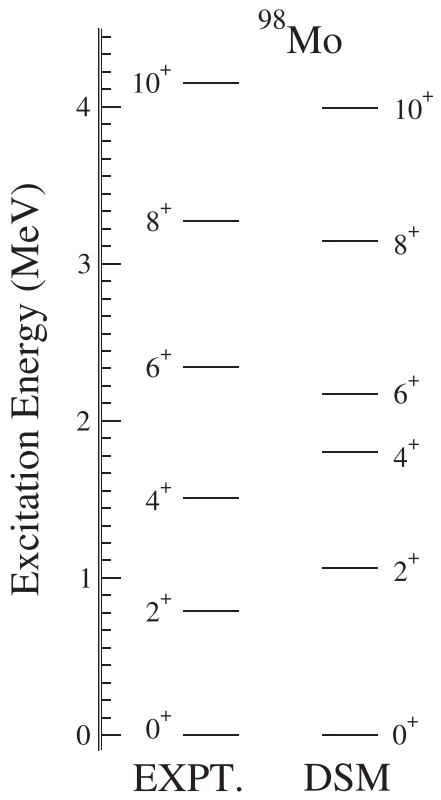

Figure 3. The ground band observed for ^{98}Mo is compared with the DSM predicted values. The experimental data are taken from [46].

As effective charges from shell model calculations in ^{100}Mo are not available, we took the effective charges for these nuclei to be 1.6e and 1.0e for protons and neutrons following our past work [29]; see also [47]. Systematic studies of B(E2) values in the ^{100}Mo region will be performed in future to determine more reliable set of effective charges in this region.

5. Conclusions

The recently observed neutral-current coherent elastic neutrino–nucleus scattering data, as well as those expected to be measured at the designed CEνNS experiments with other nuclear detectors, offer the possibility to constrain the parameter space of several models going beyond the standard model which assume vector and scalar mediators.

To this aim, various neutrino (and anti-neutrino) sources, including laboratory and astrophysical neutrinos, may be employed. Of particular importance are the non-standard reactions of the neutrinos emitted during core-collapse supernovae explosions, during the thermonuclear reactions taking place in the interior of the Sun, as well as in the Earth's atmosphere, with the sensitive nuclear detectors of XENON1T, XENONnT, DARWIN, RES-NOVA and other experiments.

Our present predictions on the ^{98,100}Mo, may be of help towards this direction since, as it is known, these isotopes are prominent detection media. They have been employed previously

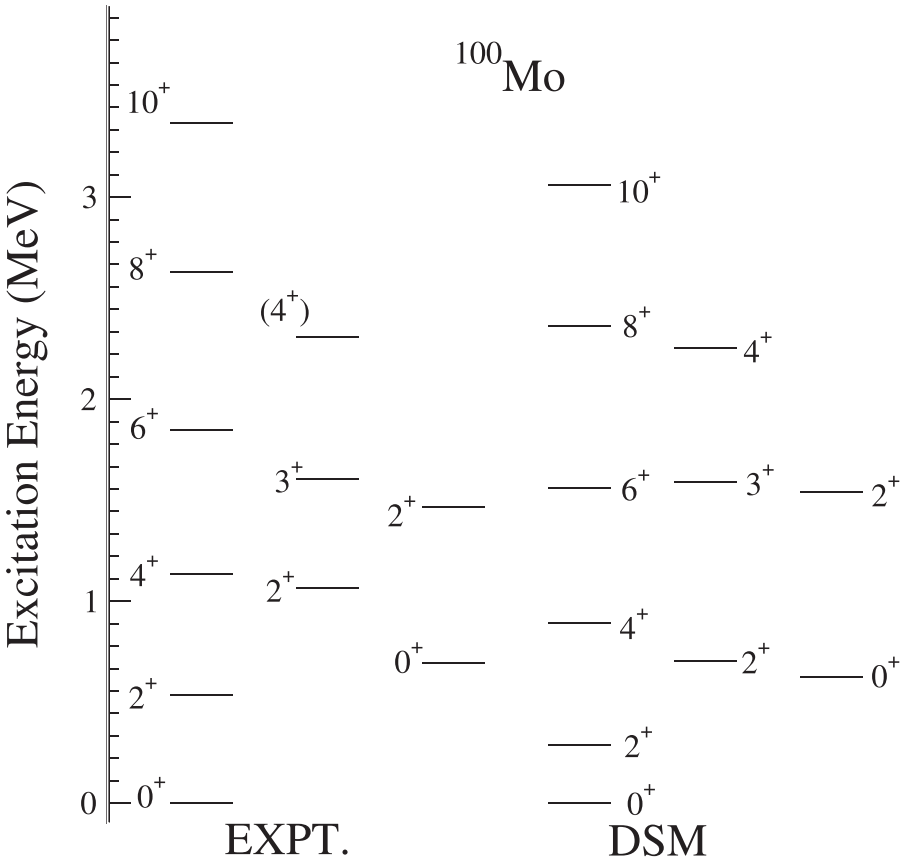

Figure 4. The collective bands observed for ^{100}Mo is compared with the DSM predicted values. The experimental data are taken from [46].

in appreciably sensitive detectors (for the detection of neutrinoless double beta decay, dark matter and neutrinos) in the MOON and NEMO experiments.

6. Results and discussions

One of our goals in this work was to calculate the incoherent differential cross sections for each multipole state included in the chosen model space of the ^{98,100}Mo isotopes. This was done by evaluating the transition matrix elements entering equations (5) and (6) through the use of the deformed SM wave function $\Phi^J_M(\eta)$ defined in equation (13).

As it is known, in spherical shell model the quenching factor is necessary to be considered [45]. It has been shown [48] that, for transfer reactions the quenching factor can be less than 0.4 as shown in figure 1 of their paper. Suhonen [49] in his shell model calculations for Mo takes the value $g_A^{\rm eff} = 0.60$ corresponding to a quenching factor of the value 0.36. As mentioned previously, the DSM is an approximation to shell model. Moreover, we found that if we use the quenching factor 0.35 (as defined by Kay *et al* [48]) we get almost similar results with those obtained by using QRPA.

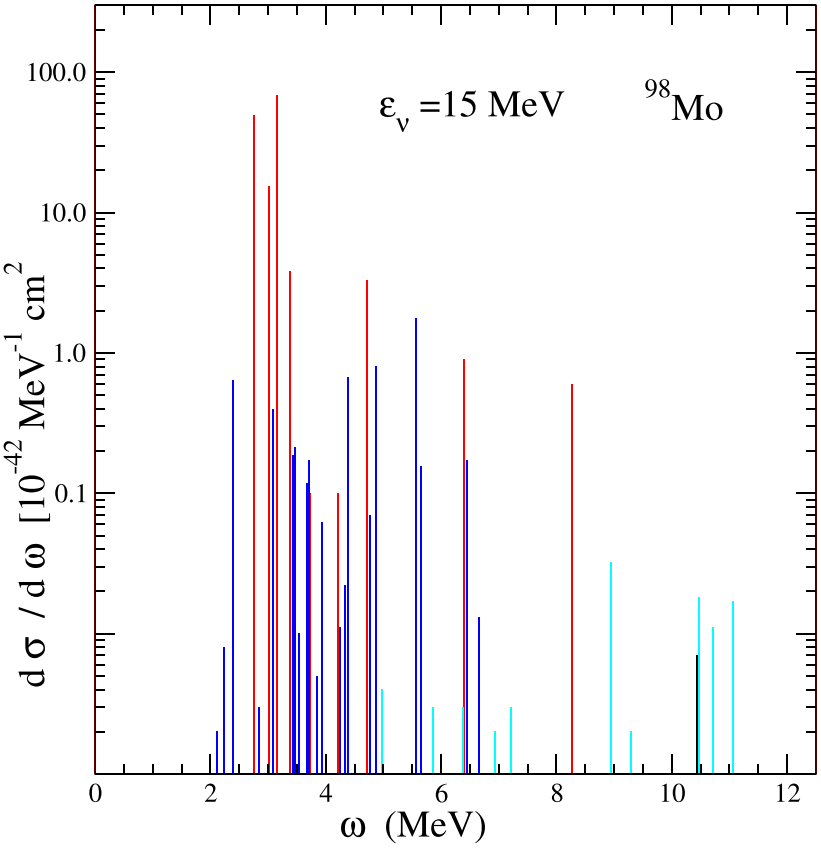

Figure 5. The differential cross section as a function of the excitation energy ω for ^{98}Mo at incoming neutrino energy $\epsilon_\nu = 15$ MeV for different excited states. The contribution of the excitation to $J = 1^+$ state is represented by red, to $J = 2^+$ by blue, to $J = 1^-$ by black, and to $J = 2^-$ by cyan.

In figure 5, the differential cross section as a function of the excitation energy ω for the ^{98}Mo is illustrated. The incoming neutrino energy is assumed to be $\epsilon_\nu = 15$ MeV which may give rise to different excited states lying up to this energy from the ground state level. As can be seen, the contribution of the multipolarities $J = 1^+$ (represented by red), $J = 2^+$ (represented by blue), $J = 1^-$ (represented by black), and $J = 2^-$ (represented by cyan) are the most important ones. For this neutrino energy ϵ_ν, other higher spin multipolarities contribute negligibly.

A similar picture for the incoherent differential cross sections is obtained for the ^{100}Mo isotope, see figure 6 where the contribution of the multipolarities $J = 1^+$ (in red), $J = 2^+$ (in blue), $J = 1^-$ (in black), and $J = 2^-$ (in cyan) are shown.

Assuming that the quenching factor is 0.35, the coherent differential cross section comes out to be 1506.2 for ^{98}Mo, while for ^{100}Mo the corresponding value 1692.9. Furthermore, for the incoherent channel in the case of ^{100}Mo, DSM predicts fourteen 1^+ states in the chosen model space. We find that the basic operators Σ'^J, Σ''^J, Δ^J and Ω^J contribute to this multipolarity. We also find that the contribution of the 1^+ multipole at $\omega = 3.14$ MeV is the

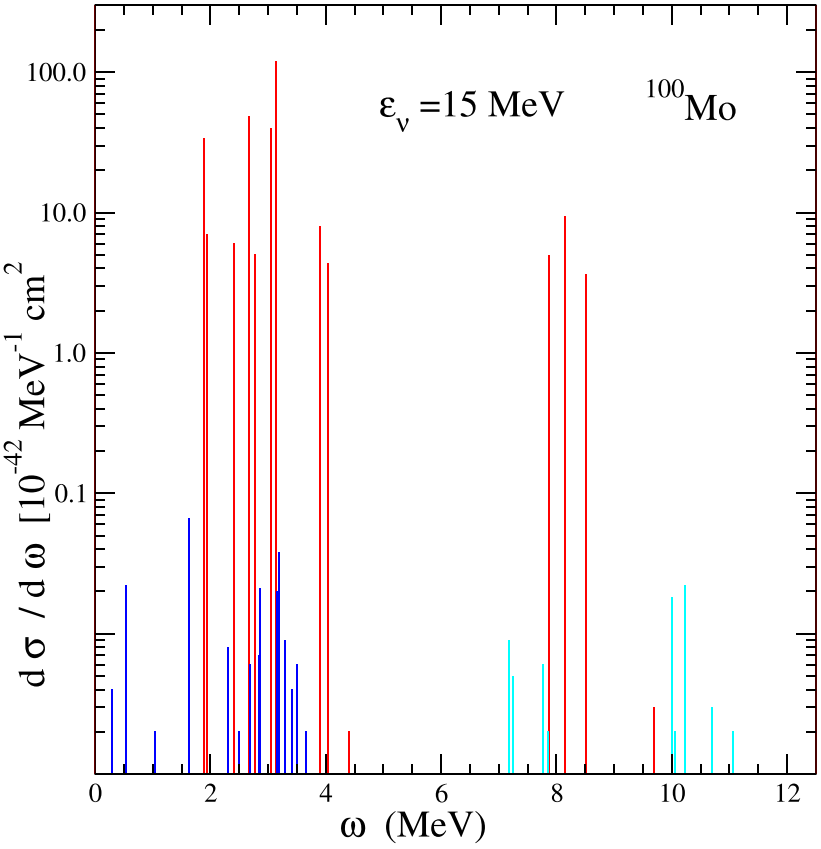

Figure 6. The differential cross section as a function of the excitation energy ω for ^{100}Mo at incoming neutrino energy $\epsilon_\nu = 15$ MeV for different excited states. The contribution of the excitation to $J = 1^+$ state is represented by red, to $J = 2^+$ by blue, to $J = 1^-$ by black, and to $J = 2^-$ by cyan.

Table 1. Coherent, Incoherent and total differential cross section of neutrino scattering off the ^{98,100}Mo detector isotopes. The portion of the Coherent into the total cross section is also listed.

Isotope	Coherent	Incoherent	Total	Coherent/total (%)
^{98}Mo	1506.2	147.7	1653.9	91.07 (%)
^{100}Mo	1692.9	290.0	1982.9	85.38 (%)

largest and has the value 120. For ^{98}Mo, we find that in DSM there are nine $K = 1^+$ levels. The contribution of the multipole 1^+ that occurs at 3.159 MeV is highest (the most pronounced one) having the value 69.

In table 1, we tabulate the coherent, incoherent and total differential cross section that comes out of our present calculation for each of the detector isotopes, ^{98}Mo and ^{100}Mo. In addition, the ratio of the measured coherent cross section over the total cross section, which is

a useful quantity, is listed in this table. By glancing at table 1, we may conclude that, possible measurements of the coherent cross section by the ongoing or designed CEvNS experiments (see discussion in the Introduction) with the use of Mo as detector medium, will offer the possibility to compare the cross sections of table 1 with the experimental results.

We note that, our cross sections correspond only to the Standard Model (SM) ν-nucleus interactions since, in our present work we did not consider contributions coming from BSM interactions. It is worth remarking that in other BSM electroweak processes where the coherent channel is also possible, e.g. the muon-to-electron conversion in nuclei (see e.g. [50, 51]) the portion of the coherent branching ratio into the total one represents also about the 85%–90% of the total rate.

Closing, as can be seen from equation (11) of [4], the SM part of the cross section could be separated out of the BSM part. This means that, by measuring the coherent part using Mo detector, one can derive stringent constraints on the particle model parameters coming, from the Mo detector. Such constraints may restrict further the parameter space of the relevant BSM scenarios related to the neutral current coherent neutrino nucleus scattering and shed more light towards explaining the part of the event rate measured at ORNL by the COHERENT experiments [5–7]. As has been discussed in [4], the coherent data cannot be explained within the SM of the electroweak interactions. Moreover, the measurements of Mo detector combined with our present predictions may help in answering some key questions related to neutrino properties and provide understanding of some BSM theories.

Acknowledgments

The author TSK wishes to acknowledge financial support from the Association for Advancement of Research on Open Problems (OPRA Association, Tel Aviv, Israel) in Nuclear Physics and Particle Physics, project No 83 241/ELKE-UoI. Also, the author RS is thankful to SERB of Department of Science and Technology (Government of India) for financial support. The publication of the article in OA mode was financially supported by HEAL-Link. Thanks are due to PC Srivastava for some useful correspondence.

Data availability statement

All data that support the findings of this study are included within the article (and any supplementary files).

Appendix

The definitions of the eight multipole operators $\hat{M}_J$, $\hat{L}_J$, $\hat{T}^{el}_J$, $\hat{T}^{\rm mag}_J$, $\hat{M}^5_J$, $\hat{L}^5_J$, $\hat{T}^{el5}_J$ and $\hat{T}^{\rm mag5}_J$, where the superscript 5 refers to the axial vector components of the hadronic current, are as follows:

$$\hat{M}^{\rm Coul}_{JM}(q\mathbf{r}) = F_1^Z \hat{M}^J_M(q\mathbf{r}), \qquad \hat{L}_{JM}(q\mathbf{r}) = \frac{q_0}{q}\hat{M}^{\rm Coul}_{JM}(q\mathbf{r}),$$

$$\hat{T}^{el}_{JM}(q\mathbf{r}) = \frac{q}{M}\left[F_1^Z \Delta'^J_M(q\mathbf{r}) + \frac{1}{2}(F_1^Z + 2MF_2^Z)\Sigma^J_M(q\mathbf{r})\right],$$

$$i\hat{T}^{\rm mag}_{JM}(q\mathbf{r}) = \frac{q}{M}\left[F_1^Z \Delta^J_M(q\mathbf{r}) + \frac{1}{2}(F_1^Z + 2MF_2^Z)\Sigma'^J_M(q\mathbf{r})\right],$$

$$i\hat{M}^5_{JM}(q\mathbf{r}) = \frac{q}{M}\left[F_A^Z \Omega^J_M(q\mathbf{r}) + \frac{1}{2}F_A^Z \Sigma'^J_M(q\mathbf{r})\right],$$

$$-i\hat{L}^5_{JM}(q\mathbf{r}) = F_A^Z \Sigma'^J_M(q\mathbf{r}),$$

$$-i\hat{T}^{el5}_{JM}(q\mathbf{r}) = F_A^Z \Sigma'^J_M(q\mathbf{r}),$$

$$\hat{T}^{\rm mag5}_{JM}(q\mathbf{r}) = F_A^Z \Sigma^J_M(q\mathbf{r}).$$

where we neglect the pseudo scalar form factor. In equation (6), the first three and last multipole operators have normal parity, $\pi = (-)^J$ while others have abnormal parity, $\pi = (-)^{J+1}$.

ORCID iDs

V K B Kota https://orcid.org/0009-0008-2975-0426
T S Kosmas https://orcid.org/0000-0001-6245-6589

References

[1] Freedman D Z 1974 Coherent effects of a weak neutral current *Phys. Rev.* D **9** 1389
[2] Scholberg K 2006 Prospects for measuring coherent neutrino–nucleus elastic scattering at a stopped-pion neutrino source *Phys. Rev.* D **73** 033005
[3] Tsakstara V and Kosmas T S 2011 Analyzing astrophysical neutrino signals using realistic nuclear structure calculations and the convolution procedure *Phys. Rev.* C **84** 064620
[4] Papoulias D K and Kosmas T S 2018 COHERENT constraints to conventional and exotic neutrino physics *Phys. Rev.* D **97** 033003
[5] COHERENT Collaboration *et al* 2017 Observation of coherent elastic neutrino–nucleus scattering *Science* **357** 1123
[6] COHERENT Collaboration *et al* 2022 Measurement of the coherent elastic neutrino–nucleus scattering cross section on CsI by COHERENT *Phys. Rev. Lett.* **129** 081801
[7] COHERENT Collaboration *et al* 2021 First measurement of coherent elastic neutrino–nucleus scattering on argon *Phys. Rev. Lett.* **126** 012002
[8] Colaresi J, Collar J, Hossbach T, Lewis C, Yocum K and (NCC-1701) 2022 and measurement of coherent elastic neutrino–nucleus scattering from reactor antineutrinos *Phys. Rev. Lett.* **129** 211802
[9] CONNIE Collaboration *et al* 2022 Search for coherent elastic neutrino–nucleus scattering at a nuclear reactor with CONNIE 2019 data *J. High Energy Phys.* JHEP05(2022)017
[10] CONUS Collaboration *et al* 2022 Novel constraints on neutrino physics beyond the standard model from the CONUS experiment *J. High Energy Phys.* JHEP05(2022)085
[11] νGeN Collaboration *et al* 2022 First results of the νGeN experiment on coherent elastic neutrino–nucleus scattering *Phys. Rev.* D **106** L051101
[12] MINER Collaboration *et al* 2017 Background studies for the MINER coherent neutrino scattering reactor experiment *Nucl. Instrum. Meth.* A **853** 53
[13] Billard J *et al* 2017 Coherent neutrino scattering with low temperature bolometers at chooz reactor complex *J. Phys* G **44** 105101
[14] Strauss R *et al* 2017 The ν-cleus experiment: a gram-scale fiducial-volume cryogenic detector for the first detection of coherent neutrino–nucleus scattering *Eur. Phys. J.* C **77** 506

[15] Wong H T- 2015 Taiwan eXperiment on neutrinO—history and prospects *Universe* **3** 22
[16] Ricochet collaboration *et al* 2015 Results from a prototype TES detector for the ricochet experiment arXiv:2304.14926v1
[17] Fernandez-Moroni G *et al* 2021 The physics potential of a reactor neutrino experiment with skipper CCDs: measuring the weak mixing angle *J. High Energy Phys.* JHEP03(2021)186
[18] SBC, CEνNS Theory Group at IF-UNAM Collaboration *et al* 2021 Physics reach of a low threshold scintillating argon bubble chamber in coherent elastic neutrino–nucleus scattering reactor experiments *Phys. Rev.* D **103** L091301
[19] Baxter D *et al* 2020 Coherent elastic neutrino–nucleus scattering at the european spallation source *J. High Energy Phys.* JHEP02(2020)123
[20] CCM Collaboration *et al* 2022 First dark matter search results from coherent CAPTAIN-mills *Phys. Rev.* D **106** 012001
[21] Chasioti V C and Kosmas T S 2009 A unified formalism for the basic nuclear matrix elements in semi-leptonic processes *Nucl. Phys.* A **829** 234
[22] Janka H T 2017 Neutrino emission from supernovae arXiv:1702.08713
[23] Tsakstara V and Kosmas T S 2011 Low-energy neutral-current neutrino scattering on ^{128,130} Te isotopes *Phys. Rev.* C **83** 054612
[24] Tsakstara V and Kosmas T S 2012 Nuclear responses of ^{64,66} Zn isotopes to supernova neutrinos *Phys. Rev.* C **86** 044618
[25] Pattavina L, Ferreiro Iachellini N and Tamborra I 2020 Neutrino observatory based on archaeological lead *Phys. Rev.* D **102** 063001
[26] Suliga A M and Tamborra I 2021 Astrophysical constraints on nonstandard coherent neutrino–nucleus scattering *Phys. Rev.* D **103** 083002
[27] Donnelly T W and Walecka J D 1976 Semi-leptonic weak and electromagnetic interactions with nuclei: Isoelastic processes *Nucl. Phys.* A **274** 368
[28] Donnelly T W and Peccei R D 1979 Neutral current effects in nuclei *Phys. Rep.* **50** 1
[29] Kota V K B and Sahu R 2016 *Structure of Medium Mass Nuclei: Deformed Shell Model and Spin-Isospin Interacting Boson Model* (CRC Press)
[30] Ydrefors E, Balasi K G, Kosmas T S and Suhonen J 2012 Detailed study of the neutral-current neutrino–nucleus scattering off the stable Mo isotopes *Nucl. Phys.* A **896** 1
[31] Doe P *et al* 2003 Neutrino studies in ^{100}Mo and MOON -Mo observatory of neutrinos *Nucl. Phys.* A **721** 517c
[32] Balasi K G, Kosmas T S, Divari P C and Ejiri H 2010 Neutral current reaction cross sections for the stable ^{100}Mo isotope *J. Phys. Conf. Ser.* **203** 012101
[33] Arnold R *et al* 2005 First results of the search for neutrinoless double-beta decay with the NEMO 3 detector *Phys. Rev. Lett.* **95** 182302
[34] Shima T *et al* 2008 MOON for next-generation neutrino-less double-beta decay experiment; present status and perspective *J. Phys. Conf. Ser.* **120** 052055
[35] Ydrefors E, Mustonen M T and Suhonen J 2010 MQPM description of the structure and beta decays of the odd $A = 95$, 97 Mo and Tc isotopes *Nucl. Phys.* A **842** 33
[36] Ydrefors E, Balasi K G, Kosmas T S and Suhonen J 2011 The nuclear response of ^{95,97} Mo to supernova neutrinos *Nucl. Phys.* A **866** 67
[37] Balasi K G, Ydrefors E and Kosmas T S 2011 Theoretical study of neutrino scattering off the stable even Mo isotopes at low and intermediate energies *Nucl. Phys.* A **868-869** 82
[38] Perdrisat C F, Punjabi V and Vanderhaeghen M 2007 Nucleon electromagnetic form factors *Prog. Part. Nucl. Phys.* **59** 694
[39] Sahu R and Kota V K B 2017 Deformed shell model study of event rates for WIMP-^{73}Ge scattering *Mod. Phys. Lett.* A **32** 1750210
[40] Papoulias D K, Sahu R, Kosmas T S, Kota V K B and Nayak B 2018 Novel neutrino-floor and dark matter searches with deformed shell model calculations 2018 ID6 *Adv. High Energ. Phys.* **2018** 031362
[41] Papoulias D K, Kosmas T S, Sahu R, Kota V K B and Hota M 2020 Constraining nuclear physics parameters with current and future COHERENT data *Phys. Lett.* B **800** 135133
[42] Sahu R, Papoulias D K, Kota V K B and Kosmas T S 2020 Elastic and inelastic scattering of neutrinos and weakly interacting massive particles on nuclei *Phys. Rev.* C **102** 035501
[43] Sahu R, Kota V K B and Kosmas T S 2021 Event rates for the scattering of weakly interacting massive particles from ^{23}Na and ^{40}Ar *Particles* **4** 75

[44] Kosmas T S, Kota V K B, Papoulias D K and Sahu R 2021 Coherent elastic neutrino–nucleus scattering (*CEνNS*) event rates for Ge, Zn, and Si detector materials *Phys. Rev.* C **104** 064618
[45] Dey P *et al* 2022 Experimental investigation of high-spin states in ^{90}Zr *Phys. Rev.* C **105** 044307
[46] Information on http://nndc.bnl.gov/
[47] Coraggio L, De Angelis L, Fukui T, Gargano A and Itaco N 2017 Calculation of gamow-teller and two-neutrino double-β decay properties for ^{130}Te and ^{136}Xe with a realistic nucleon-nucleon potential *Phys. Rev.* C **95** 064324
[48] Kay B P, Schiffer J P and Freeman S J 2013 Quenching of cross sections in nucleon transfer reactions *Phys. Rev. Lett.* **111** 042502
[49] Suhonen J T 2017 Value of the axial-vector coupling strength in β and $\beta\beta$ decays: a review *Front. Phys.* **5** 55/1–35
[50] Kosmas T S, Faessler A and Vergados J D 1997 The new limits of the neutrinoless (μ^-, e^-) conversion branching ratio *J. Phys. G: Nucl. Part. Phys.* **23** 693–703
[51] Kosmas T S 2002 Current nuclear physics issues in studying the neutrinoless (μ^-, e^-) conversion in nuclei *Prog. Part. Nucl. Phys.* **48** 307–16